Rotational wave-packet imaging of molecules

S. Ramakrishna and Tamar Seideman
Department of Chemistry, Northwestern University, 2145 Sheridan Road, Evanston, Illinois 60208-3113, USA
(Received 18 September 2012; published 15 February 2013)

We propose and illustrate numerically the possibility of imaging rotational wave packets in angular space and time by using different pump-probe spectroscopic techniques. A general theoretical framework to perform such rotational mapping is derived and three specific spectroscopies, namely, birefringence, high harmonic generation, and angle-resolved photoelectron spectroscopy, are numerically explored. All three approaches are shown to provide direct mapping of the rotational coherences of molecules but they are not equivalent; comparison of their results yields interesting insights into their relative merits. Finally, we illustrate the role played by the symmetry of the molecular orbitals in determining the quality of the images generated by high harmonic and photoelectron signals. The potential of rotational imaging as a route to both intramolecular coupling mechanisms and the interaction of molecules with different environments is discussed.

DOI: 10.1103/PhysRevA.87.023411 PACS number(s): 33.80.−b, 42.65.Ky, 34.50.Gb

I. INTRODUCTION

Wave-function imaging has been the subject of increasing excitement in recent years [1–4]. Several well-established approaches provide a view of the amplitude associated with stationary electronic wave functions [1–3] or the probability density of vibrational wave functions [4]. Yet more interestingly, the possibility of extracting information about the phase and modulus of wave functions [5] or wave packets [6–12] has been demonstrated via different experimental techniques.

The spatiotemporal evolution of a wave packet arises due to the coherent superposition of several stationary eigenstates. One can image the time-dependent probability distribution in coordinate space or go further and extract the amplitude and relative phases of all the individual states that comprise the wave packet, amounting to quantum state tomography or holography [7,8]. The possibility of imaging Rydberg electronic wave packets in atoms, by measuring the underlying amplitudes and phases, for instance, was illustrated in Refs. [9,10,12,13]. More recently, tomography of an electronic wave packet of a molecule has been performed using high-order harmonics [14]. A complete quantum state reconstruction of vibrational wave packets has been demonstrated in Refs. [7,11] and time-dependent vibrational probability distributions have been imaged using laser-induced fluorescence in Refs. [15,16] and via Coulomb explosion methods in Refs. [17–20].

A particularly interesting case is that of rotational wave packets, namely, broad coherent superpositions of eigenstates of the total material angular momentum. Rotationally broad coherent wave packets are formed via sequential rotational excitation induced by the interaction of a moderately intense laser pulse with the (permanent, transition, or induced) dipole of the molecular system [21,22]. The phase relations between the rotational components of the wave packet guarantee that the molecular axis (axes) will align with the field polarization vector(s). In the nonadiabatic limit, where the pulse is short with respect to the rotational period(s) of the molecule, the superposition of rotational states coherently excited during the pulse continues to beat after the turn-off, leading to an early field-free alignment period and a subsequent revival pattern. In the case of linear or symmetric top molecules, the early field-free alignment is precisely reconstructed at multiples of the rotational period. Experimentally, coherent wave-packet alignment has been explored via a variety of approaches, including Coulomb explosion techniques [23–25], birefringence studies [26,27], resonant-enhanced multiphoton ionization (REMPI) [28,29], x-ray spectroscopy [30], and strong-field approaches to the determination of the refractive index [31,32].

To date, the vast majority of studies of rotational wave packets have focused on applications of the associated sharp alignment in fields ranging from attosecond pulse generation [33] and orbital tomography [1,3,14] to control of unimolecular chemistry [34] and electron transport via molecular junctions [35,36]. The interest in rotationally broad wave packets as such, however, has been noted. In particular, it was illustrated that rotational coherences can serve to explore intramolecular coupling mechanisms, such as rotation-vibration coupling [37–42]. More interestingly, rotational coherences were shown to contain unique information regarding the interaction of solvated molecules with their environment, hence, potentially, a route to the dissipative properties of exotic media [43,44]. In the weak-field limit, nonadiabatic alignment reduces to the method of rotational coherence spectroscopy—a well-established approach to determining rotational constants (and hence molecular structures) that was successfully applied to a large variety of complex molecules [45–47]. Our interest in rotational wave-packet imaging is thus not only for the extension of the imaging concept to new modes of motion but also as a potential diagnostic tool in molecular research.

A question that has been debated in the past in the context of strong-field-induced alignment, and is relevant also to the discussion below, is that of a quantitative measure of the degree of alignment. The vast majority of the theoretical and experimental studies have used the expectation value of $\cos^2\theta$ in the time-evolving wave packet to that end, where θ is the polar Euler angle between the space-fixed and body-fixed z axes. The expectation value $\langle\cos^2\theta\rangle$ is proportional (up to a constant) to the second moment of the rotational distribution, hence providing a convenient and transferable one-dimensional (1D) measure that is accessible by several experiments. It was noted in the past, however, that the complete rotational distribution (which contains all moments) provides a wealth of information that is not exhibited

in $\langle \cos^2\theta \rangle$ [48]. In particular, the latter observable exhibits only second-order rotational coherences (since $\cos^2\theta$ couples angular momentum states J, J' only for $|J - J'| = 0,2$), whereas the rotational probability exhibits all high-order rotational coherences. This argument will be made sharper through discussion of Figs. 1(a) and 1(b) below. As shown in the next section, $\langle \cos^2\theta \rangle$ is a measure of the probability that the molecular axis is aligned along the space-fixed z-axis and properly approximates that probability when the rotational wave packet contains no more than second order coherences ($|J - J'| = 2$). In order, however, to appreciate the rotational dynamics at angles other than $\theta = 0$ vs time, or the structure arising from higher than second order interferences, the complete rotational probability distribution is needed. Here, the Coulomb explosion imaging approach has proved a useful, readily visualized route to exploring additional facets of the rotational distribution. While informative and successful, this approach requires careful choice of the molecule [very specific bond(s) need to break through the explosion], tight control of the experimental conditions, and nontrivial analysis, [25] in addition to being limited to the gas phase. The development of a more general and less experimentally demanding imaging approach is thus pertinent.

In the present work we propose three different approaches to image the time-evolving probability density of rotational wave packets, develop a theoretical framework to simulate these images, explore their information content, and compare their resolution. Throughout we restrict attention to linear molecules. In the next section we provide a qualitative discussion of the rotational imaging concept that serves to motivate our approach and place the different imaging approaches introduced in context. Section III derives the theory, beginning with the case of Raman-induced polarization spectroscopy (RIPS) (Sec. III A), proceeding to high harmonic generation (HHG) (Sec. III B), and ending with angle-resolved photoelectron spectroscopy (PES) (Sec. III C). Our results are presented in Sec. IV, and the final section summarizes our conclusions, pointing to avenues for future research. Several derivations that we expect to interest our readers but are not essential to follow the text are deferred to the Appendix.

II. BASIC PRINCIPLE OF ROTATIONAL IMAGING

We consider a pump-probe scenario, where the pump is a linearly polarized, moderately intense pulse of duration that is short with respect to the rotational period. This pulse serves to excite a rotationally broad, coherent wave packet via sequential, angular momentum nonconserving transitions. The time-evolving rotational probability density is imaged by means of a time-delayed probe, whose nature and mathematical description are discussed in the next section. The rotational density operator $\tilde{\rho}_r(\tau)$, a vector in Liouville space, subsequent to the pump pulse, is given as

$$\tilde{\rho}_r(\tau) = \sum_{JMJ'M'} \rho_{JMJ'M'}(\tau) |JM\rangle\langle J'M'|, \tag{1}$$

where $\rho_{JMJ'M'}$ represent elements of the rotational density matrix, J and M being the quantum numbers corresponding to the total material angular momentum and its projection onto the space-fixed z axis, respectively, and τ is the time delay with respect to the pump pulse. The rotational probability density $\rho_r(\theta,\phi,\tau)$, a scalar in angular coordinate space, is thus

$$\begin{aligned}\rho_r(\theta,\phi,\tau) &= \langle\theta,\phi|\tilde{\rho}_r|\theta,\phi\rangle \\ &= \sum_{JMJ'M'} \rho_{JMJ'M'}(\tau) Y_{JM}(\theta,\phi) Y^*_{J'M'}(\theta,\phi),\end{aligned} \tag{2}$$

where $\langle\theta,\phi|JM\rangle = Y_{JM}(\theta,\phi)$ are spherical harmonics, θ is the polar Euler angle between the space-fixed and body-fixed z axes, and ϕ is the azimuthal angle of rotation about the space-fixed z axis. In Eq. (2) the latter axis is taken to be the pump-field polarization vector, but another definition will be more physically natural and mathematically convenient below.

Spectroscopic signals from rotational wave packets are shown below to be expressible quite generally in terms of the expectation value of a rotational operator in the time-evolving rotational density. The functional form of the rotational operator, denoted $\mathcal{M}(\theta,\phi)$ below, as a function of the Euler angles, depends on the direction of the polarization vector of the probe pulse and the experimental probe envisioned; several specific examples are derived in the next section. The observable optical signal is then

$$\begin{aligned}I_{\text{signal}}(\tau,\gamma) \propto \Bigg| \sum_{JMJ'M'} \rho^{\gamma}_{JMJ'M'}(\tau) \int \sin\theta d\theta d\phi\, Y_{JM}(\theta,\phi) \\ \times Y^*_{J'M'}(\theta,\phi)\mathcal{M}(\theta,\phi)\Bigg|^2,\end{aligned} \tag{3}$$

where γ is the angle between the space-fixed z axis and the alignment pulse polarization vector. (In the case of photoelectron spectroscopy, discussed in Sec. III C, the signal depends on the rotational density, rather than on its square.) Rotational imaging could be envisioned as sampling the rotational probability of Eq. (2) by rotating the probe polarization vector with respect to the rotational density quantization axis in Eq. (2). An equivalent and mathematically more convenient description entails rotation of the pump polarization, and hence the rotational probability density, with respect to a fixed spatial axis that is defined by the probe (*vide infra*) and serves as the quantization axis (the space-fixed z axis). Thus, the probability density can be equivalently written

$$\rho^{\gamma}_r(\theta,\phi,\tau) = \rho_r(\theta - \gamma,\phi,\tau). \tag{4}$$

As the pump polarization axis is rotated with respect to the space-fixed z axis, M is no longer conserved and the elements of the density matrix are parametrized by rotation angle γ.

In the limit where the rotational operator is nearly as sharply peaked as the Dirac-delta function, that is, $\mathcal{M}(\theta,\phi) \approx \delta(\theta - \theta_0)\delta(\phi - \phi_0)/\sin\theta$ about a specific set of Euler angles θ_0,ϕ_0,

$$\begin{aligned}I_{\text{signal}}(\tau,\gamma) &\approx \Bigg| \sum_{JMJ'M'} \rho^{\gamma}_{JMJ'M'}(\tau) Y_{JM}(\theta_0,\phi_0) Y^*_{J'M'}(\theta_0,\phi_0)\Bigg|^2 \\ &\approx \left|\rho^{\gamma}_r(\theta_0,\phi_0,\tau)\right|^2 = |\rho_r(\theta_0 - \gamma,\phi_0,\tau)|^2,\end{aligned} \tag{5}$$

i.e., the signal is proportional to the squared modulus of the rotational probability density along a certain direction specified by the (experimentally variable) angle γ for any time τ. In reality the rotational operator $\mathcal{M}(\theta,\phi)$ will not be as sharply peaked as a Dirac-delta function. Rather, one expects

a moderately peaked function that will allow the signal to probe not the precise rotational density as a function of the Euler angles but rather a coarse-grained version of it. We will find below that the probe may peak about an angle $\theta_0 \neq 0$ (while exhibiting an angular breadth). This nonzero peak angle translates into a shift of the image (considered as a function of γ) with respect to the probability density map. Often, however, the rotational operator in Eq. (3) will be independent of the azimuthal angle ϕ, $\mathcal{M}(\theta,\phi) = \mathcal{M}(\theta)$. In that case the spectroscopic signal does not have a preferred direction in azimuthal space and integration of the signal over ϕ leads to disappearance of the θ_0 rotational shift in the obtained image. In either case, in the limit of a sharply defined $\mathcal{M}(\theta)$, the (γ,τ) dependence of $I^{\gamma}_{\text{signal}}(\tau)$ maps the (θ,τ) dependence of the rotational probability density.

To further motivate our discussion, and also to serve as a basis for testing the fidelity of the imaging techniques introduced below, we show in Figs. 1(a) and 1(b) the rotational probability density of Eq. (2) versus the polar Euler angle θ and the time delay τ. Here and below we consider specifically the cases of N_2 and O_2 molecules, as these two systems have been intensively studied in the alignment context, both experimentally and numerically, and since they represent two common and very different molecular symmetries. Shown to the left of Figs. 1(a) and 1(b) are the corresponding averaged alignment measures $\langle\cos^2\theta\rangle(\tau)$. As discussed in

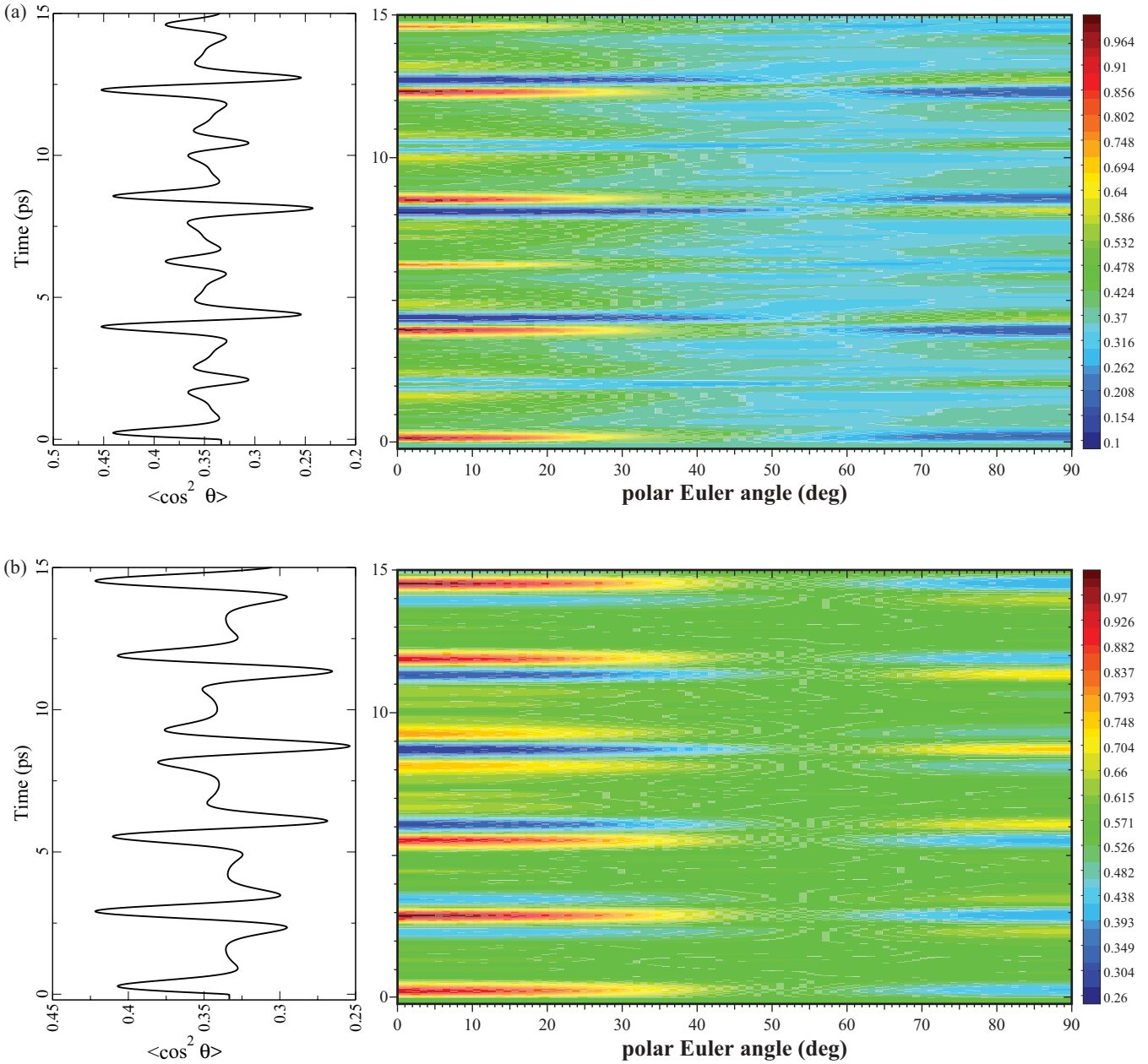

FIG. 1. (Color online) The rotational probability density for (a) N_2 and (b) O_2 vs time and the polar Euler angle θ compared with the averaged alignment measure $\langle\cos^2\theta\rangle$ (left). The Gaussian pump pulse of 25 fs pulse width and a peak intensity of 75 TW cm^{-2} for N_2 and 25 TW cm^{-2} for O_2 and a rotational temperature of 30 K is used in the calculations.

Sec. I, $\langle\cos^2\theta\rangle(\tau)$ exhibits several, but not all, features of the time-evolving wave packet. The expectation value of $\cos^2\theta$ in the rotational density of Eq. (2) provides a coarse-grained image of the rotational probability density about the $\theta = 0$ point. It therefore conveys the probability of the molecular axis being parallel to the space-fixed z axis at any given time in an averaged sense. Although it is an extremely useful and a very popular observable for quantifying the degree of alignment with respect to the space-fixed z axis, it mirrors the probability density only in the vicinity of $\theta = 0$. Further, as Fig. 1 illustrates, the probability distribution exhibits a structure that is not observed in $\cos^2\theta$ since $\cos^2\theta$ couples only rotational levels J and J' with $|J - J'| = 0,2$ and hence exhibits only second-order rotational interferences, whereas a wave packet excited by a pulse of sufficient amplitude and duration contains a broad range of high-order rotational coherences. The contour figures characterizing the rotational probability densities for the two molecules considered motivate the development of rotational wave-packet imaging approaches and will also serve in the analysis of the results below.

III. THEORY

To realize the imaging of the rotational probability density of linear molecules we now turn to deriving expressions for the signals corresponding to different potential rotational imaging experiments. Specifically, we derive the form of the rotational operator, $\mathcal{M}(\theta,\phi)$ in Eq. (3), for three time-resolved spectroscopic techniques. The functional dependence of $\mathcal{M}(\theta,\phi)$ on θ and ϕ differs in the three cases and determines the resolution of the rotational image in angular space.

A. Extended Raman-induced polarization spectroscopy

An optical spectroscopy that has emerged in recent years as a powerful approach to probe field-free alignment dynamics induced by a strong pulse is one that is similar to the optical Kerr effect and measures the birefringence produced by the alignment of the molecular sample [26,27]. The experimental geometry for this spectroscopy, termed Raman-induced polarization spectroscopy (RIPS), consists of a linearly polarized aligning pulse followed by a time-delayed, linearly polarized probe pulse whose polarization vector is tilted with respect to the aligning pulse by $\pi/4$. The signal is collected along a direction $\hat{n}$ that is perpendicular to the probe polarization vector and lies in the plane defined by the pump and probe polarization vectors. The observed signal $I_{\rm RIPS}$ is proportional to the squared magnitude of the expectation value of the $\hat{n}$ projection of the induced dipole operator $\vec{\mu}_{\rm ind}$,

$$I_{\rm RIPS}(\tau) \approx |\langle\hat{n}\cdot\vec{\mu}_{\rm ind}\rangle|^2 = |{\rm Tr}\{\hat{n}\cdot\vec{\mu}_{\rm ind}\,\tilde{\rho}_r(\tau)\}|^2. \qquad (6)$$

In the context of conventional RIPS experiments, where the pump polarization direction is fixed with respect to that of the probe and the observation direction, it is conventional (and convenient) to define the pump pulse polarization vector as the space-fixed z axis, with the plane spanned by the pump and probe polarization vectors defining the space-fixed z-y plane. Thus, $\hat{\varepsilon}_{\rm pr} = \varepsilon_z\hat{z} + \varepsilon_y\hat{y}$ with $\varepsilon_z = \varepsilon_y$ and the polarization vector of the analyzer is $\hat{n} = n_z\hat{z} + n_y\hat{y}$, where $n_z = -n_y$. Here and below $\hat{\varepsilon}_{\rm pr}$ denotes a unit vector along the probe field polarization direction. Equation (6) can thus be recast as

$$I_{\rm RIPS}(\tau) \approx \left|\sum_{JMJ'M'}\rho_{JMJ'M'}(\tau)\int\sin\theta d\theta d\phi Y_{JM}(\theta,\phi) \times Y^*_{J'M'}(\theta,\phi)(\cos^2\theta - \sin^2\theta\sin^2\phi)\right|^2. \qquad (7)$$

Given, however, that the pump field is linearly polarized along the space-fixed z axis, the projection of the angular momentum on the z axis, given by the quantum number M, is conserved and hence $\langle\sin^2\phi\rangle = 0$. Thus, the conventional RIPS signal is proportional to $\langle\cos^2\theta\rangle$. Past work on the characterization of the alignment induced by moderately intense laser pulses has successfully applied RIPS to measure and control the time-evolving expectation value $\langle\cos^2\theta\rangle$ [26,27].

As noted above, although $\langle\cos^2\theta\rangle$ has been the most popular measure of strong-field-induced alignment, it provides only the second moment of the rotational wave packet and hence does not convey the complete information contained in the wave packet. Here we envision a modified approach, based on the standard RIPS concept [27], where the pump-field polarization vector is stepwise rotated with respect to the weak-field, time-delayed probe polarization vector, the latter remaining perpendicular to $\hat{n}$, to record the polarization signal versus the time delay and the angle (γ) between the space-fixed z axis and the pump polarization vector ($\hat{\varepsilon}_{\rm pu}$), $\gamma = \cos^{-1}\hat{\varepsilon}_{\rm pu}\cdot\hat{z}$. As the pump polarization vector is rotated with respect to the space-fixed z axis ($\langle\sin^2\phi\rangle \neq 0$), the rotational operator $\mathcal{M}(\theta,\phi) = \cos^2\theta - \sin^2\theta\sin^2\phi$ peaks around both $\theta = 0$ and $\theta = \pi/2$. This leads to a mirror reflection of the probability density map about a symmetry plane passing through $\theta = \pi/4$. If, however, one records only the component of the RIPS signal that is parallel to the space-fixed z axis (e.g., by using a second analyzer), the rotational density mapping is significantly improved. It is readily shown that the intensity of the z component of the RIPS signal is given by

$$\begin{aligned} I^{\parallel}_{\rm RIPS}(\tau,\gamma) &\approx \left|\sum_{JMJ'M'}\rho^{\gamma}_{JMJ'M'}(\tau)\int\sin\theta d\theta d\phi,\right. \\ &\quad \left.\times Y_{JM}(\theta,\phi)Y^*_{J'M'}(\theta,\phi)\cos^2\theta\right|^2 \\ &= \left|\sum_{JMJ'M'}\rho_{JMJ'M'}(\tau)\int\sin\theta d\theta d\phi,\right. \\ &\quad \left.\times Y_{JM}(\theta-\gamma,\phi)Y^*_{J'M'}(\theta-\gamma,\phi)\cos^2\theta\right|^2, \qquad (8) \end{aligned}$$

irrespective of the relative orientation of the pump polarization vector in space (that is, for all γ). Equation (8) illustrates that the γ dependence of the extended RIPS signal thus generated maps the θ dependence of the rotational probability density. One can also use the perpendicular component of the RIPS signal alone in mapping the rotational density but, as will be discussed in the next section, the same information (with the same resolution) is obtained using either component.

B. High-order harmonic signals

High harmonic signals from nonadiabatically aligned molecules have been the topic of intensive study over the past 7 years, and continue to offer new questions for research. High harmonic generation (HHG) is well understood in terms of a three-step process [49,50], wherein ionization takes place close to the maximum of the electric field, generating a free-electron wave packet in the continuum that follows the electric-field oscillations. If the field is linearly (or close to linearly) polarized, the electronic wave packet will revisit the vicinity of the core, and, with a small probability, undergo recombination, thus emitting harmonics of the driving field. The intense (and very fruitful) interest in HHG from nonadiabatically aligned linear molecules has been largely inspired by the early report of tomographic imaging of molecular orbitals based on measurements of harmonic spectra at a series of angles between the alignment and ionization polarization vectors [1]. Of specific interest for the focus of the present study are subsequent experiments that recorded harmonic signals as a function of the time delay between an alignment (pump) pulse and a subsequent ionization (probe) pulse, seeking to understand the functional form of the τ-dependent spectra and their relation to molecular properties. While tomographic imaging of orbitals remains a topic of controversy, it has been shown that HHG from aligned molecules contains interesting structural and dynamical information about the underlying molecular system.

In particular, of relevance to the present work, Refs. [51,52] point out the information content of harmonic signals with regard to the rotational coherences responsible for the wave-packet alignment. Specifically, the theory of Refs. [51,52] predicts that harmonic spectra would exhibit much higher-order fractional rotational revivals than have been observed so far, due to the involvement of rotational operators of more complex form than the conventional $\cos^2\theta$ in determining the spectrum (see the discussion of Sec. I; explicit forms of such operators are provided below). Very recently, these predictions were confirmed experimentally [53]. An interesting question, thus, is the extent to which, and the way in which, HHG can serve to map the rotational density of wave packets.

The theory of HHG from aligned molecules is derived elsewhere [51,52] and is not reproduced here. We provide only the results that are required in order to reformulate the signal in the general form (3). The intensity of the emitted harmonic polarized along a direction $\hat{n}$ is proportional to the squared magnitude of the Fourier transform of the expectation value

$$\mathrm{Tr}\{\vec{\mu}\cdot\hat{n}\,\tilde{\rho}(\tau,t)\} = \mathrm{Tr}\{\vec{\mu}\cdot n_z\hat{z}\,\tilde{\rho}(\tau,t)\} + \mathrm{Tr}\{\vec{\mu}\cdot n_y\hat{y}\,\tilde{\rho}(\tau,t)\}, \tag{9}$$

where $\vec{\mu}$ is the dipole operator, $\tilde{\rho}(\tau,t)$ is the complete (electronic rovibrational) density operator of the molecule, $\hat{y}$ and $\hat{z}$ are unit vectors along the space-fixed y and z axes, respectively, and we consider the common setup of HHG experiments from aligned molecules, where the alignment (pump) pulse polarization vector, the ionization (probe) polarization vector, and the detection direction are coplanar. The polarization vector of the ionization (probe) pulse defines the space-fixed z axis and the common plane of the polarization vectors is taken to define the (y,z) plane with $\gamma = \cos^{-1}(\hat{\varepsilon}_{\mathrm{pu}}\cdot\hat{\varepsilon}_{\mathrm{pr}}) = \cos^{-1}(\hat{\varepsilon}_{\mathrm{pu}}\cdot\hat{z})$. The two components of the signal amplitude in Eq. (9) for linear molecules are given as [54]

$$\begin{aligned}&\mathrm{Tr}\{\vec{\mu}\cdot n_z\hat{z}\,\tilde{\rho}(\tau,t)\}\\ &= \int d\hat{R}\,\rho_r^{\gamma}(\theta,\phi,\tau)\Bigg\{\cos^2\theta\sum_{ll'k_l} Y_{lk_l}(\theta,\chi)\\ &\quad\times Y^*_{l'k_l}(\theta,\chi)F_{\parallel}(l,l',k_l,t)\\ &\quad+\sin^2\theta\sum_{ll'k_l} Y_{lk_l}(\theta,\chi)Y^*_{l'k_l}(\theta,\chi)F_{\perp}(l,l',k_l,t)\Bigg\}+\mathrm{c.c.}\end{aligned} \tag{10}$$

and

$$\begin{aligned}&\mathrm{Tr}\{\vec{\mu}\cdot n_y\hat{y}\,\tilde{\rho}(\tau,t)\}\\ &= \int d\hat{R}\,\rho_r^{\gamma}(\theta,\phi,\tau)\sin\phi\sin\theta\cos\theta\Bigg\{\sum_{ll'k_l} Y_{lk_l}(\theta,\chi)\\ &\quad\times Y^*_{l'k_l}(\theta,\chi)F_{\parallel}(l,l',k_l,t)\\ &\quad-\sum_{ll'k_l} Y_{lk_l}(\theta,\chi)Y^*_{l'k_l}(\theta,\chi)F_{\perp}(l,l',k_l,t)\Bigg\}+\mathrm{c.c.},\end{aligned} \tag{11}$$

where $\hat{R}$ denotes collectively the Euler angles of rotation, $\hat{R}=(\theta,\phi,\chi)$, and χ is the azimuthal angle of rotation about the body-fixed z axis. In Eqs. (10) and (11) l and k_l are the electronic angular momentum and its projection onto the body-fixed z axis, and the electronic-vibrational factors are given as

$$\begin{aligned}&F_{\parallel(\perp)}(l,l'k_l,t)\\ &= \frac{2}{\pi}i^{l-l'-1}\sum_{v_c}|\langle v|v_c\rangle|^2\rho_{vv}(\tau)\int dk\,\langle b|\mu_{\parallel(\perp)}|\Phi_{lk_l}\rangle\\ &\quad\times\int^t dt'\rho_{bb}(t')\varepsilon_{\mathrm{pr}}(t')\langle\Phi_{l'k_l}|\mu_{\parallel(\perp)}|b\rangle e^{-iS(t,t')},\end{aligned} \tag{12}$$

where v and v_c denote the vibrational indexes of the bound and ionic states, respectively, ρ_{vv} and ρ_{bb} are the bound-state vibrational and electronic densities, respectively, and $S=\int_{t'}^{t}(E^{k(t'')}+E^{v_c}+I_p-E^{v_b})dt''$, I_p being the ionization potential and $E^{k(t)}$ the continuum electronic energy. As above, we reserve the variable τ to denote the delay between the alignment and probe pulses, and use t to denote time with respect to the ionization pulse. Assuming that Born-Oppenheimer separability is valid for the bound state, we express the complete probability density as

$$\rho^{\gamma}(\theta,\phi;\tau,t)=\rho_r^{\gamma}(\theta,\phi;\tau)\rho_{vv}(\tau)\rho_{bb}(t). \tag{13}$$

Thus, the $\rho_r(\theta,\phi,\tau)$ in Eqs. (10) and (11) contains the response of the rotational subspace to the alignment pulse and evolves on rotational time scales, whereas the $F_{\parallel(\perp)}(l,l'k_l,t)$ contain the response of the electronic subspace to the ionization pulse and evolve on the electronic time scales. Although in

principle the partial-wave expansion in Eqs. (10) and (11) involves an infinite series, in practice it often converges rapidly.

Equations (10) and (11) thus formulate the harmonic spectra in the general form (3), where, however, the rotational operator $\mathcal{M}(\theta,\phi)$ depends not only on the geometry of the experiment, as in the RIPS case, but involves also the electronic symmetry of the bound state of the molecule. Each electronic-vibrational factor $F_{\parallel(\perp)}$ describes (i) the process of tunnel ionization of the bound electronic state $|b\rangle$ into the continuum partial waves $|\Phi_{l,k_l}\rangle$ subject to the interaction of the probe laser field $\varepsilon_{\rm pr}(t')$ with the dipole moment $\mu_{\parallel(\perp)}$ parallel (perpendicular) to the molecular axis, (ii) propagation of the electron in the continuum under the action of the laser field, in the course of which its phase S and momentum k evolve, and finally (iii) recombination with the bound state. Since the electronic dynamics is entangled with the rotational dynamics (although evolving on widely disparate time scales), the rotational response depends on both the electron energy (hence the harmonic order) and the orbital symmetry. On the one hand, this feature may serve to extract valuable information about the electronic dynamics from measurements of the τ dependence of harmonic spectra [53]. On the other, it suggests that the resolution of rotational mapping based on HHG will be system dependent.

The two cases most intensively studied in the context of HHG from aligned molecules are those of the N_2 and the O_2 molecules. In the former case, Eqs. (10) and (11) reduce to

$$\mathrm{Tr}\{\vec{\mu}_{\rm N_2}\cdot n_z\hat{z}\,\tilde{\rho}_{\rm N_2}(\tau,t)\} \propto \int d\hat{R},\rho_r^{\gamma}(\theta,\phi;\tau)\cos^4\theta F_{\parallel}(1,1,0,t) \tag{14}$$

and

$$\mathrm{Tr}\{\vec{\mu}_{\rm N_2}\cdot n_y\hat{y}\,\tilde{\rho}_{\rm N_2}(\tau,t)\} \propto \int d\hat{R}\,\rho_r^{\gamma}(\theta,\phi;\tau)\cos^3\theta\sin\theta\sin\phi F_{\parallel}(1,1,0,t), \tag{15}$$

where attention is restricted to the first (dominating) term in the partial-wave expansion. In the latter case, one finds

$$\begin{aligned}\mathrm{Tr}\{\vec{\mu}_{\rm O_2}\cdot\hat{n}_z\hat{z}\,\tilde{\rho}_{\rm O_2}(\tau,t)\} \approx \int d\hat{R}\,\rho_r^{\gamma}(\theta,\phi;\tau)\{&\cos^2\theta[Y_{11}Y_{11}^*(F_{\parallel}(1,1,-1,t)+F_{\parallel}(1,1,1,t))\\ &+Y_{11}Y_{31}^*(F_{\parallel}(1,3,-1,t)+F_{\parallel}(1,3,1,t))+\cdots]\\ &+\sin^2\theta[Y_{10}Y_{10}^*F_{\perp}(1,1,0,t)+Y_{10}Y_{30}^*F_{\perp}(1,3,0,t)+\cdots]\}+\text{c.c.}\end{aligned} \tag{16}$$

and

$$\begin{aligned}\mathrm{Tr}\{\vec{\mu}_{\rm O_2}\cdot\hat{n}_y\hat{y}\,\tilde{\rho}_{\rm O_2}(\tau,t)\} \approx \int d\hat{R}\,\rho_r^{\gamma}(\theta,\phi;\tau)\cos\theta\sin\theta\sin\phi\{&[Y_{11}Y_{11}^*(F_{\parallel}(1,1,-1,t)\\ &+F_{\parallel}(1,1,1,t))+Y_{11}Y_{31}^*(F_{\parallel}(1,3,-1,t)+F_{\parallel}(1,3,1,t))+\cdots\\ &-[Y_{10}Y_{10}^*F_{\perp}(1,1,0,t)+Y_{10}Y_{30}^*F_{\perp}(1,3,0,t)+\cdots]\}+\text{c.c.},\end{aligned} \tag{17}$$

where several terms, whose magnitudes do not differ widely, have been retained. As a consequence of orbital symmetry the first term (the $l=1,k_l=0$ partial wave) dominates in the case of N_2, whereas several initial terms contribute for O_2, including the perpendicular component of the dipole element. Thus, in the case of N_2 the rotational operator $\mathcal{M}(\theta,\phi)$ [see Eq. (3)] does not differ qualitatively from its analog in the RIPS case, $\cos^4\theta$ being only slightly better spatially defined than $\cos^2\theta$. In the case of O_2, by contrast, higher-order rotational moments can dominate and better spatial resolution may be expected, depending, however, on the harmonic order.

C. Angle-resolved photoelectron spectroscopy

Time- and angle-resolved photoelectron spectroscopy (PES) has been proposed in the past as a route to the rotational composition of wave packets [37–42,55,56] and their time-evolving electronic symmetry [41,48,57–62]. Here, the pump pulse aligns the molecule and the (weak) probe pulse leads to photoejection of electrons that are resolved with respect to both angle and energy (the latter to within the probe pulse bandwidth) and can be recorded as a function of the pump-probe time delay. As in the previous sections, we define the space-fixed z axis as the probe pulse polarization vector, $\hat{\varepsilon}_{\rm pr}=\hat{z}$, with the pump (alignment) pulse polarization vector $\hat{\varepsilon}_{\rm pr}$ defining the space-fixed zy plane and $\gamma=\cos^{-1}(\hat{\varepsilon}_{\rm pu}\cdot\hat{z})$.

The time-evolving population of ejected photoelectrons as a function of the continuum momentum $\vec{k}$ is given as

$$P_{\rm PES}(\vec{k},\{c\},\tau,t,\gamma)=\mathrm{Tr}\{|\vec{k},\{c\}\rangle\langle\vec{k},\{c\}|\tilde{\rho}^{\gamma}(\tau,t)\}, \tag{18}$$

where $\{c\}$ denotes collectively the electronic, vibrational, and rotational indices of the ion core, $\{c\}=(c,v_c,J_c,M_c)$, and the signal is proportional to the long-time limit of Eq. (18), $\lim_{t\to\infty}P_{\rm PES}(\vec{k},\{c\},\tau,t,\gamma)$. To facilitate comparison with the previous sections, we use the subscripts c to denote the ion core quantum numbers, retaining the set (b,v,J,M) to specify the bound-state quantum numbers. Equation (18) reduces to evaluating the density-matrix element pertaining to a continuum electron occupying a well-defined momentum state and

the associated rotational and vibrational density matrices of the ion core, namely, $\rho^{\gamma}_{\vec{k}\{c\},\vec{k}\{c\}}(t)$. Experimental measurements of time-resolved PES signals, however, are mostly focused on less detailed observables that are not resolved with respect to the final-state rotational and vibrational levels. Proceeding to sum Eq. (18) over the collection of quantum indexes $\{c\}$, we make use of the quantum Liouville equation as detailed in the Appendix to find

$$P_{\rm PES}(\vec{k},\tau,t,\gamma)=\sum_{\{c\}}\rho^{\gamma}_{\vec{k}\{c\},\vec{k}\{c\}}(\tau,t)=\sum_{\{c\}\{b\}}-\frac{i}{\hbar}\langle\{b\}|\vec{\mu}\cdot\hat{\varepsilon}_{\rm pr}|\vec{k},\{c\}\rangle\int_{-\infty}^{t}dt'\varepsilon_{\rm pr}(t')\rho^{\gamma}_{\vec{k}\{c\},\{b\}}(\tau,t')+{\rm H.c.}, \tag{19}$$

where $\{b\}$ labels the bound electronic state along with its associated rotational-vibrational manifold, $\{b\}=(b,v,J,M)$, $\vec{\mu}$, as above, is the molecular dipole vector, and $\hat{\varepsilon}_{\rm pr}$ is a unit vector in the direction of polarization of the probe pulse, $\hat{\varepsilon}_{\rm pr}=\hat{z}$. As Eq. (19) illustrates, the population of photoelectrons in a continuum state $|\vec{k},\{c\}\rangle$ is determined by the coherence term $\rho^{\gamma}_{\vec{k}\{c\},\{b\}}$, which is an off-diagonal density-matrix element. Making use of the quantum Liouville equation and following the derivation of the Appendix, we arrive at an approximate expression for the element of interest,

$$\rho^{\gamma}_{\vec{k}\{c\},\{b\}}(\tau,t')\approx\sum_{\{b'\}}\frac{i}{\hbar}\langle\vec{k},\{c\}|\vec{\mu}\cdot\hat{\varepsilon}_{\rm pr}|\{b'\}\rangle\int_{-\infty}^{t'}dt''\varepsilon_{\rm pr}(t'')\rho^{\gamma}_{\{b'\},\{b\}}(\tau,t'')e^{\frac{i}{\hbar}(E^{\{c\}}-E^{\{b\}})(t''-t')}, \tag{20}$$

where $E^{\{c\}}$ and $E^{\{b\}}$ denote the continuum and bound-state energy eigenvalues and the probe pulse has been expressed as $\vec{\varepsilon}_{\rm pr}(t)=\hat{\varepsilon}_{\rm pr}\varepsilon_{\rm pr}(t)$. In deriving Eq. (20), we have assumed that (1) the pump and probe pulses do not overlap in time and hence the pump field does not affect the photoelectron dynamics, and (2) the probe intensity is below saturation, hence continuum coherences and populations are negligible as compared to the bound-state analogs.

Using Eqs. (19) and (20) we have

$$\begin{aligned}P_{\rm PES}(\vec{k},\tau,t,\gamma)\approx\frac{2}{\hbar^2}{\rm Re}\sum_{\{c\}\{b\}\{b'\}}\Bigg\{&\langle\{b\}|\vec{\mu}\cdot\hat{\varepsilon}_{\rm pr}|\vec{k},\{c\}\rangle\langle\vec{k},\{c\}|\vec{\mu}\cdot\hat{\varepsilon}_{\rm pr}|\{b'\}\rangle\int_{-\infty}^{t}dt'\varepsilon_{\rm pr}(t')\\&\times\int_{-\infty}^{t'}dt''\varepsilon_{\rm pr}(t'')\rho^{\gamma}_{\{b'\},\{b\}}(\tau,t'')e^{\frac{i}{\hbar}(E^{\{c\}}-E^{\{b\}})(t''-t')}\Bigg\}.\end{aligned} \tag{21}$$

We proceed by factorizing the bound component of the density matrix into electronic, vibrational, and rotational components in the spirit of the Born-Oppenheimer approximation as

$$\rho^{\gamma}_{\{b\},\{b'\}}(\tau,t'')=\rho_{bb}(t'')\rho^{\gamma}_{JMJ'M'}(\tau)\rho_{vv'}(\tau), \tag{22}$$

where, as in the above, ρ_{bb} is the electronic, $\rho^{\gamma}_{JMJ'M'}$ the rotational, and $\rho_{vv'}$ the vibrational density-matrix elements of the bound state. Given that the bound-state rotational and vibrational density-matrix elements are not changed during the brief ionization time, the equation of motion for the rotational and vibrational density-matrix elements are determined by a quantum Liouville equation that involves solely the pump pulse. Finally, neglecting the molecular-ion rotational energies as compared to the electronic energies in the exponential term (for O_2, for instance, the ratio of these energies is 10^{-5}), and making use of the closure property of spherical harmonics,

$$\sum_{J_cM_c}\langle\theta,\phi\big|J_cM_c\rangle\langle\theta',\phi'\big|J_cM_c\rangle^{*}=\delta(\theta-\theta')\delta(\phi-\phi')/\sin\theta, \tag{23}$$

one finds

$$\begin{aligned}P_{\rm PES}(\vec{k},\tau,t,\gamma)\approx\frac{2}{\hbar^2}{\rm Re}\Bigg\{&\sum_{v_cvv'}\rho_{vv'}(\tau)\langle v|v_c\rangle\langle v_c|v'\rangle\sum_{JMJ'M'}\rho^{\gamma}_{JMJ'M'}(\tau)\int d\hat{R}Y_{JM}(\theta,\phi)Y^{*}_{J'M'}(\theta,\phi)\\&\times\Big[\langle b|\mu_{\parallel}|\vec{k}\rangle\langle\vec{k}|\mu_{\parallel}|b'\rangle\cos^2\theta+\langle b|\mu_{\perp}|\vec{k}\rangle\langle\vec{k}|\mu_{\perp}|b'\rangle\sin^2\theta\Big]\int_{-\infty}^{t}dt'\varepsilon_{\rm pr}(t')\\&\times\int_{-\infty}^{t'}dt''\varepsilon_{\rm pr}(t'')\rho_{bb}(t'')e^{\frac{i}{\hbar}(E^{\{c\}}-E^{\{b\}})(t''-t')}\Bigg\},\end{aligned} \tag{24}$$

where $\mu_{\parallel}$ and $\mu_{\perp}$ are the components of the dipole operator parallel and perpendicular to the molecular axis and we have assumed that the matrix elements of these operators in the electronic basis [the $\langle b|\mu_{\parallel}|\vec{k}\rangle$ in Eq. (24)] are independent of the vibrational coordinates.

The continuum electron wave function is conveniently expanded in a partial-wave series as

$$\langle\boldsymbol{Q}|\vec{k}\rangle=\sqrt{\frac{2}{\pi}}\sum_{lm_lk_l}i^{l}D^{l*}_{m_lk_l}(\hat{R})Y^{*}_{lm_l}(\hat{k})\Phi_{lk_l}(k,\boldsymbol{Q},t), \tag{25}$$

where $\boldsymbol{Q}$ denotes the electronic coordinates with respect to the body-fixed frame, l and k_l are the electronic angular momentum and its body-fixed z projection (see Sec. III B), $\Phi_{lk_l}(k,\boldsymbol{Q},t)$ is the corresponding partial wave with $k=|\vec{k}|$, and m_l denotes the projection of l onto the space-fixed z axis. Using Eq. (25) in Eq. (24) we have

$$P_{\rm PES}(\vec{k},\tau,t,\gamma) \approx \frac{4}{\pi\hbar^2}{\rm Re}\left\{\sum_{v v' v_c}\rho_{v'v}(\tau)\langle v|v_c\rangle\langle v_c|v'\rangle \sum_{ll'k_l m_l m_l'} Y^*_{lm_l}(\hat{k})Y_{l'm_l'}(\hat{k}) \sum_{JMJ'M'}\rho^{\gamma}_{JMJ'M'}(\tau)\right.$$
$$\times\int d\hat{R}\, Y_{JM}(\theta,\phi)Y^*_{J'M'}(\theta,\phi)D^{l'}_{m_l'k_l}(\hat{R})D^{l*}_{m_l k_l}(\hat{R})\left[\cos^2\theta\mu_{\parallel}(l,k_l)\mu^*_{\parallel}(l',k_l)+\sin^2\theta\mu_{\perp}(l,k_l)\mu^*_{\perp}(l',k_l)\right]$$
$$\left.\times\, i^{l-l'}\int_{-\infty}^{t}dt'\varepsilon_{\rm pr}(t')\int_{-\infty}^{t'}dt''\varepsilon_{\rm pr}(t'')\exp\left[\frac{i}{\hbar}(E^{\{c\}}-E^{\{b\}})(t''-t')\right]\rho_{b'b}(t'')\right\}, \tag{26}$$

where the partial-wave electronic dipole matrix elements are defined as $\mu_{\parallel}(l,k_l)=\langle\phi_b|\mu_{\parallel}|\Phi_{lk_l}\rangle$ and $\mu_{\perp}(l,k_l)=\langle\phi_b|\mu_{\perp}|\Phi_{lk_l}\rangle$. Considerable simplification has been obtained in Eqs. (24) and (26) from the fact that cross products of dipole matrix elements such as $\mu_{\parallel}(l,k_l)\mu^*_{\perp}(l',k_l)$ cancel out. Equation (26) is of the form (3), where, however, the rotational operator $\mathcal{M}(\theta,\phi)$ is a complex function of the Euler angles. Similar to the HHG case of Sec. III B, $\mathcal{M}(\theta,\phi)$, and hence the resolution of the mapping depend on both the molecular symmetry and the electron dynamics.

To gain qualitative insight into the form of Eq. (26), and hence its potential to serve as a rotational imaging, it is useful to introduce several assumptions and approximations that will simplify and make more explicit the functional dependence of $\mathcal{M}(\theta,\phi)$ on the Euler angles. Assuming that the pump pulse is detuned far from vibrational transition frequencies (which is the case in most alignment experiments), vibrational coherences in the bound state are not excited and the double sum over v,v' reduces to a single term (corresponding to the initial vibrational state in experiments where the parent state is vibrationally selected). The incoherent sum over v_c becomes redundant if the final vibrational state of the ion is resolved. In this situation, the long-time limit of the double integral in Eq. (26) reduces to a constant that is primarily determined by the pulse envelope. Assuming further that the detection direction [$\hat{k}$ in Eq. (26)] is chosen to lie along the space-fixed z axis (defined above by the probe polarization direction), $\hat{k}=\hat{\varepsilon}_{\rm pr}=\hat{z}$, the double sum over m_l,m_l' reduces to a single term, $m_l=m_l'=0$, and one finds for the PES signal $I_{\rm PES}(\vec{k},\tau,t,\gamma)=\lim_{t\to\infty}P_{\rm PES}(\vec{k},\tau,t,\gamma)$,

$$I_{\rm PES}(k,\hat{k}=\hat{z},\tau,\gamma)$$
$$\propto {\rm Re}\left\{\sum_{ll'k_l} i^{l-l'}\sum_{JMJ'M'}\rho_{JMJ'M'}(\tau)\right.$$
$$\times\int d\hat{R}\, Y_{JM}(\theta,\phi)Y^*_{J'M'}(\theta,\phi)Y_{lk_l}(\theta,\chi)Y^*_{l'k_l}(\theta,\chi)$$
$$\left.\times\left[\cos^2\theta\mu_{\parallel}(l,k_l)\mu^*_{\parallel}(l',k_l)+\sin^2\theta\mu_{\perp}(l,k_l)\mu^*_{\perp}(l',k_l)\right]\right\}, \tag{27}$$

where, in order to simplify the notation and focus on the components that are relevant for our purpose, we have omitted all the constants. Equation (27) is reminiscent of the expression for the amplitude of the HHG signal along the space-fixed z axis, given by Eq. (10). A similar series of rotational operators is obtained for the two cases, the important difference between them arising from the respective dipole matrix elements. As discussed in the context of HHG above, although in principle the partial-wave expansion of the continuum electronic wave function is infinite, in practice it often converges rapidly. Assuming, as in the HHG case, that due to the orbital symmetry of N_2 and O_2 the first term (the $l=1,k_l=0$ partial wave) dominates for the former whereas several initial terms contribute for the latter, we find

$$I^{\rm N_2}_{\rm PES}(k,\hat{k}=\hat{z},\tau,\gamma)$$
$$\propto {\rm Re}\left\{\int d\hat{R}\,\rho^{\gamma}_r(\theta,\phi,\tau)\cos^4\theta|\mu_{\parallel}(l=1,k_l=0)|^2\right\}, \tag{28}$$

$$P^{\rm O_2}_{\rm PES}(k,\hat{k}=\hat{z},\tau)$$
$$\propto {\rm Re}\left\{\int d\hat{R}\,\rho^{\gamma}_r(\theta,\phi,\tau)(\cos^2\theta\{Y_{11}Y^*_{11}(|\mu_{\parallel}(1,1)|^2\right.$$
$$+|\mu_{\parallel}(1,-1)|^2)-([Y_{11}Y^*_{31}(\mu_{\parallel}(1,1)\mu^*_{\parallel}(3,1)$$
$$+\mu_{\parallel}(1,-1)\mu^*_{\parallel}(3,-1))]+{\rm c.c.})+\cdots\}$$
$$+\sin^2\theta\{Y_{10}Y^*_{10}|\mu_{\perp}(1,0)|^2-Y_{10}Y^*_{30}\mu_{\perp}(1,0)\mu^*_{\perp}(3,0)$$
$$\left.-Y_{30}Y^*_{10}\mu_{\perp}(3,0)\mu^*_{\perp}(1,0)+\cdots\})\right\}, \tag{29}$$

for the O_2 symmetry. Unlike in the case of N_2, the perpendicular component of the dipole element, $\mu_{\perp}$, need not be small compared to the parallel in the case of O_2, owing to its π_g symmetry. For instance, $|\mu_{\parallel}(1,\pm1)|^2=|\mu_{\perp}(1,0)|^2$. Thus, for the setup envisioned above ($\hat{k}=\hat{\varepsilon}_{\rm pr}$), assuming that a single partial wave dominates the signal, the operator $\mathcal{M}(\theta,\phi)$ behaves as $\cos^4\theta$ in the case of N_2 and as a superposition of quadratic and quartic powers of $\cos\theta$ in the case of O_2 molecules. The former is a relatively well-defined function of θ, peaked at $\theta=0$, whereas the latter depends on the composition of the superposition. In practice, whereas the assumptions introduced in the derivation of Eq. (27) are readily realized, the assumption that a single partial wave determines the signal, Eqs. (28), is typically invalid. The response of the

images to the number of partial waves contributing to the spectrum is explored in Sec. IV C.

IV. RESULTS AND DISCUSSION

In this section we proceed to apply the theory derived in the previous section to explore possibilities of mapping the density of rotational wave packets onto experimental observables. As above, we use the N_2 and O_2 molecules as simple complementary examples. We begin in Sec. IV A with a discussion of RIPS, continue in Sec. IV B to the case of HHG, and conclude with a discussion of rotational imaging by means of PES. The rotational wave packets are created with a Gaussian pump pulse of 25 fs pulse width and a peak intensity of 75 TW cm^{-2} for N_2 and 25 TW cm^{-2} for O_2. All calculations are carried out at a relatively high rotational temperature (30 K), where about 15 rotational states are thermally populated. Since our goal is to explore a general concept, rather than to describe the properties of specific molecules, we compute the dipole matrix elements for the HHG case within the strong-field approximation and for the PES case using a Coulomb wave-function description for the continuum states. Thus, our results do not provide quantitative signals for either molecule, but can assess the potential of the proposed imaging methods, clarify their differences and similarities, and illustrate the sense in which and degree to which they depend on the system details.

A. Rotational wave-packet imaging using RIPS

Figures 2(a) and 2(b) show contour plots of the parallel component of the (extended) RIPS signal versus the pump-probe time delay τ and the angle $\gamma = \cos^{-1}(\hat{\varepsilon}_{\rm pu} \cdot \hat{z})$ between the pump polarization vector and the space-fixed z axis, calculated as detailed in Sec. III A. The rotational operator in question is $\mathcal{M}(\theta,\phi) = \cos^2\theta$, a function that is peaked at $\theta = 0$, but is a relatively broad function of θ. A comparison of Figs. 1(a) and 1(b) with Figs. 2(a) and 2(b) illustrates the concept of rotational mapping; the signal as a function of (γ,τ) reproduces the structure of the rotational density in (θ,τ) space rather faithfully, tracing the fractional revival structure as well as the structure of ρ_r in angular space. The finite angular

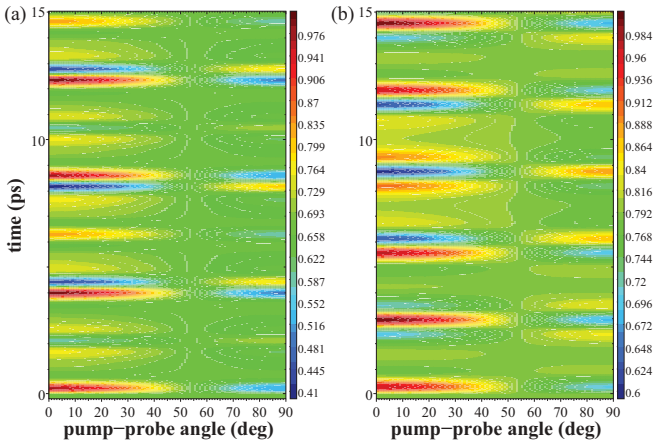

FIG. 2. (Color online) Rotational mapping using RIPS for (a) N_2, (b) O_2. The pulse and system parameters are as in Fig. 1.

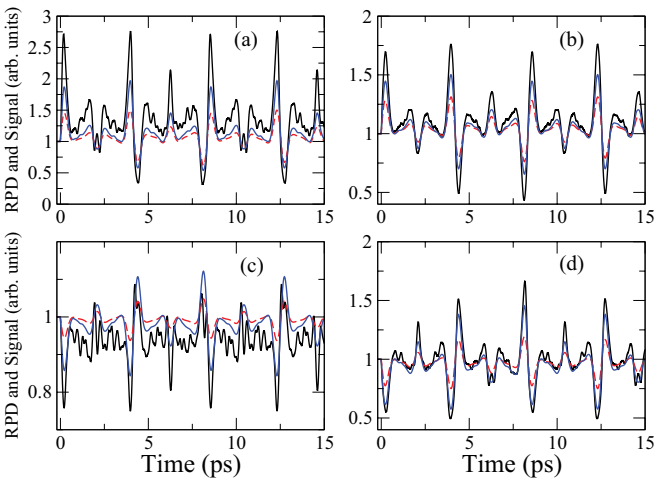

FIG. 3. (Color online) Cuts through the N_2 rotational probability distributions (RPD) of Fig. 1(a) (black) compared with cuts through the RIPS signal of Fig. 2(a) (red dashed) and the HHG signal of Fig. 5(a) (solid blue/gray) at polar angles (a) $\theta = 0$, (b) $\theta = 30^\circ$, (c) $\theta = 60^\circ$, and (d) $\theta = 90^\circ$. The rotational shift discussed in the text is included in the HHG cuts to simplify the comparison.

width of the $\mathcal{M}(\theta,\phi) = \cos^2\theta$ leads to a certain degree of coarse graining, but this is barely discerned. The result of Figs. 2(a) and 2(b) is remarkable considering the fact that it is obtained from a nonintrusive optical signal that is more general and significantly simpler to measure and analyze than imaging via Coulomb explosion. Similar results are obtained by using the component of the signal that is perpendicular to the space-fixed z axis to map the rotational density (not shown), in which case the rotational operator in question is $\mathcal{M}(\theta,\phi) = -\sin^2\theta\sin^2\phi$. The map is reversed in angular space but its resolution is unaltered.

To compare more quantitatively the RIPS signal with the rotational density, we consider, in Figs. 3 and 4, constant angle cuts of the contour plot in Figs. 2(a) and 2(b), respectively, and compare them with the temporal evolution of cuts through the contour plots of the corresponding rotational densities of N_2 and O_2, Figs. 1(a) and 1(b). The traces corresponding to the RIPS signal (red dashed curves in Figs. 3 and 4) are seen

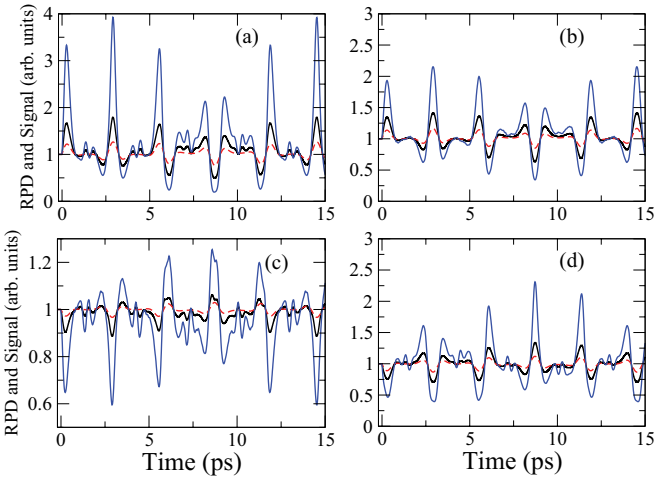

FIG. 4. (Color online) As in Fig. 3 for the case of O_2 molecules.

to capture the temporal behavior of the rotational probability (shown in black), although the fine structure of ρ_r is largely averaged out. As expected, the mapping is accurate in the regions of maximum alignment and antialignment, but suffers in the region of $\theta = \pi/3$, where the probability oscillations about the isotropic value is a minimum. The plots have been normalized with respect to the isotropic value and the smaller variations of the RIPS signal in relation to the rotational wave packet are consistent with the lesser contrast seen in the contour plots of Figs. 2(a) and 2(b).

Although the present imaging calculations are obtained specifically for the cases of N_2 and O_2, the precision with which the rotational mapping via (extended) RIPS is achieved for linear systems is molecule independent, as the rotational operator considered depends only on the geometry of the experiment. The results of Figs. 2(a) and 2(b) are therefore general.

B. Rotational wave-packet imaging using HHG

Rotational mapping via harmonic signals is conceptually similar to mapping via RIPS [see Eq. (3)], the major difference being that the rotational operator in question depends on both the detection direction [$\hat{n}$ in Eqs. (10)and (11)] and the symmetry of the molecular orbital(s) involved. The former dependence offers, as illustrated below, the possibility to tune the rotational operator so as to have advantageous spatial dependence that will improve the resolution of the mapping. The latter dependence renders the mapping less general but more controllable than the RIPS analog.

Figure 5(a) illustrates the 23rd harmonic of N_2 versus the angle $\gamma = \cos^{-1}(\hat{\varepsilon}_{\rm pu} \cdot \hat{\varepsilon}_{\rm pr}) = \cos^{-1}(\hat{\varepsilon}_{\rm pu} \cdot \hat{z})$ and the pump-probe time delay τ, as calculated within the theory of Sec. III B. As is evident from the discussion of Sec. III B, for a detection angle $\hat{n} = \hat{z}$, the resolution of the mapping is only marginally improved as compared to the case of RIPS [the rotational operator in question, $\mathcal{M}(\theta,\phi) \approx \cos^4\theta$, being only slightly better defined spatially than the one corresponding to RIPS, $\mathcal{M}(\theta,\phi) = \cos^2\theta$]. If, however, the detection direction

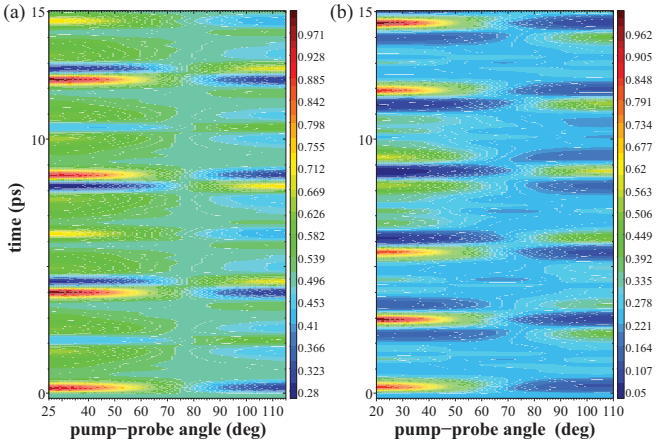

FIG. 5. (Color online) Rotational mapping using HHG for (a) N_2 and (b) O_2. The pump pulse and system parameters are as in Fig. 1, the probe pulse used to calculate the matrix elements is long (akin to continuous wave) with an intensity of 200 TW, and the 23rd harmonic is detected at an angle of 45° with respect to the probe polarization vector.

is rotated with respect to the space-fixed z axis, the rotational operator becomes a function of the azimuthal Euler angle ϕ, leading to much enhanced resolution. This is shown in Fig. 5(a), where the harmonic emission is detected at an angle of $\pi/4$ from the z axis. A comparison of Fig. 5(a) with the N_2 rotational density of Fig. 1(a) and the corresponding RIPS mapping of Fig. 2(a) illustrates much improved contrast as compared to RIPS mapping. The higher contrast is achieved due to the $\sin\phi$ term in the perpendicular component of the harmonic spectrum [see Eq. (11)]. As the signal is averaged over the entire range of the azimuthal angular space, the presence of $\sin\phi$ effectively confines it to the vicinity of the z-y symmetry plane, as the sin function peaks at $\phi = \pi/2, 3\pi/2$.

Figure 5(a) exhibits also the mapping shift predicted in Sec. III B. The shift is readily seen to arise from the perpendicular component of the emission, whose leading term is proportional to $\cos^3\theta \sin\theta \sin\phi$, a function that peaks around $\pi/6$. Combined with the parallel component, whose dominating term behaves as $\cos^4\theta$, along with other terms in the series expansion, this term leads to a peak around $\theta_0 \approx 25°$, which expresses itself as a ca. 25° shift of the map.

A more quantitative comparison of the RIPS and the HHG mapping strategies is provided in Fig. 3, where we show constant angle cuts through the contour maps of Figs. 1(a), 2(a), and 5(a). The blue (solid gray) curves, corresponding to the harmonic spectrum, illustrate the anticipated enhanced contrast as compared to the RIPS case. Except in regions where the probability density oscillations is close to its isotropic value, the HHG mapping is seen to reproduce all the gross features and much of the fine structure of the rotational density. Here too a rotational shift is noted in comparison of the cuts through the probability density and the HHG signals.

In the case of O_2 molecules, rotational imaging via harmonic signals is less mathematically transparent than in the N_2 case, due to the involvement of several terms of comparable magnitude in the partial-wave expansion of the observable [see Eqs. (16) and (17)]. At the same time, the participation of higher angular momentum states of the continuum electron results in the involvement of rotational operators that include higher powers of the trigonometric functions and are hence better localized in angular space. An example is provided in Fig. 5(b), which displays the 23rd harmonic of O_2 vs γ and τ for an emission direction $\hat{n}$ in the z-y plane, rotated by $\pi/4$ with respect to the space-fixed z axis. A comparison with the corresponding rotational density, Fig. 1(b), illustrates that the HHG mapping reproduces relatively accurately even the fine structure of ρ_r. Consistent with our expectations based on the discussion of the N_2 results above, we find that for an observation direction $\hat{n} = \hat{z}$ (not shown), the fine structure is lost, as the ϕ integration averages it out. It is the localization in the z-y plane that the perpendicular component of the signal introduces which sharpens the contrast and leads to the emergence of the fine structure. As anticipated by the discussion of Sec. II, if emission parallel to the z axis alone is considered, no rotational shift occurs as a result of averaging of the signal over all ϕ values, as the rotational operator $\mathcal{M}$ has no ϕ dependence. Similar to the case of N_2, when the emission direction includes a component perpendicular to the z axis, a rotational shift of $\theta_0 \approx 20°$ is observed [see Fig. 5(b)]. These conclusions are again substantiated by Fig. 4, which compares

constant angle cuts through the contour maps of Figs. 1(b), 2(b), and 5(b). Unlike in the case of N_2, the mapping does not lose its fine structure in regions where the probability density is small but captures all features. A similar rotational shift to that discussed above is again evident through a comparison of the cuts through the rotational probability and the HHG signal.

The results summarized in this section illustrate the relative merits of RIPS and HHG as potential rotational imaging techniques. The former is independent of the molecular details and is general, being fully determined by the experimental geometry, whereas the latter is less coarse grained and hence leads to better resolution, at least for the molecular symmetries considered here.

C. Rotational imaging via PES

As the ejected photoelectron momentum vector is angle resolved, rotational imaging via PES can in principle afford better resolution and sensitivity as compared to RIPS, similar to HHG imaging. We remark, however, that the rotational operators involved are generally different in the PES and HHG cases; the former depend on the angular momentum of the ejected electron whereas the latter depend on the angular momenta of both the ionizing and the recombining continuum states.

Figure 6(a) shows the photoelectron signal for N_2 molecules versus the angle $\gamma = \cos^{-1}(\hat{\varepsilon}_{\rm pr} \cdot \hat{z})$ (see Sec. III C) and the pump-probe time delay τ for detection parallel to the space-fixed z axis (defined in Sec. III C as the probe polarization vector), $\hat{k} = \hat{z}$. For the specific case of the N_2 molecule and the configuration considered here, the leading term in $\mathcal{M}(\theta,\phi)$ is the same in the HHG and PES cases. Accordingly, the rotational mapping obtained via PES for the N_2 molecule is quite similar to the one obtained via HHG, where an emission parallel to the space-fixed z axis is detected. Similar conclusions are reached by examining the constant angle cuts shown in Fig. 7. The PES signals are marginally sharper compared to the HHG analogs (and do not exhibit a rotational shift, as only the emission direction parallel to the z axis is detected), but their overall structure is essentially the same. Clearly, this is not a general result but rather depends on

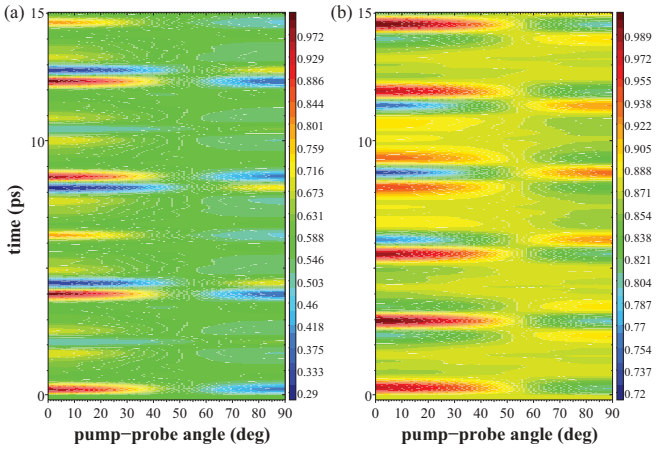

FIG. 6. (Color online) Rotational mapping using PES for (a) N_2 and (b) O_2. The pump pulse and system parameters are as in Fig. 1, and the photoelectron signal is detected at an angle of 0° with respect to the probe polarization vector.

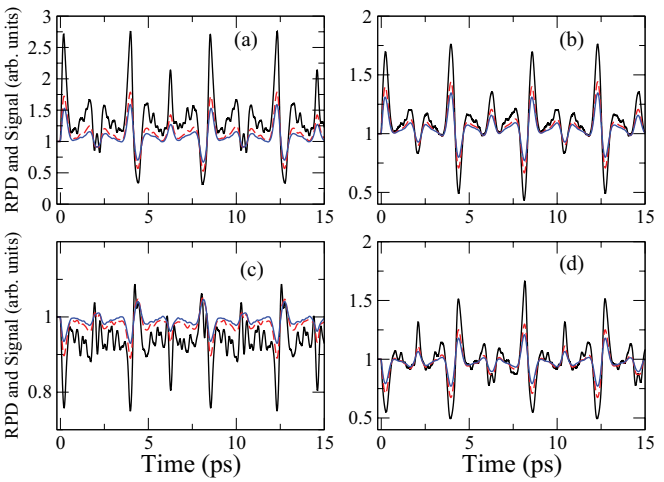

FIG. 7. (Color online) Cuts through the N_2 rotational probability distributions of Fig. 1(a) (black) compared with cuts through the PES signal of Fig. 6(a) (red dashed) and the HHG signal (solid blue/gray) at polar angles (a) $\theta = 0$, (b) $\theta = 30°$, (c) $\theta = 60°$, and (d) $\theta = 90°$. The HHG emission direction is along the probe polarization vector.

the bound orbital(s) considered and the angular momenta dominating the electronic continuum.

We conclude this section with a discussion of rotational imaging of O_2 wave packets via PES, using this example to illustrate the limitation of PES as an imaging tool while also clarifying the conditions under which PES is expected to provide enhanced contrast as compared to RIPS imaging. Figure 6(b) considers the case where the continuum electron partial-wave series is strongly dominated by the lowest allowed term, illustrating that, whereas the main features of the rotational density are reproduced, the map lacks contrast compared to that obtained by HHG and fails to capture the fine structure of the probability density. This result is accentuated in Fig. 8, which shows constant angle cuts through the probability

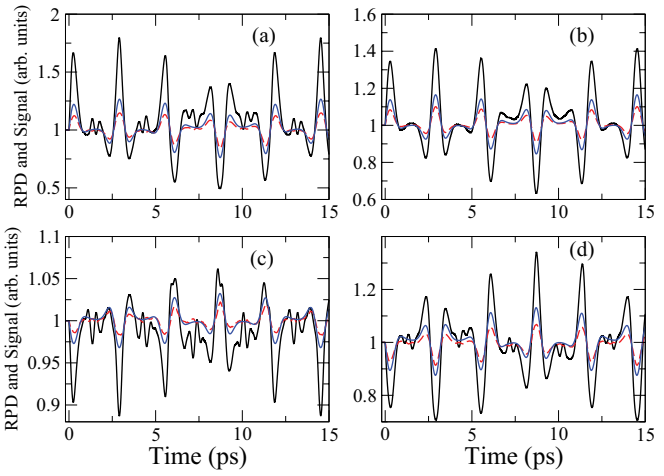

FIG. 8. (Color online) Cuts through the O_2 rotational probability distributions of Fig. 1(b) (black) compared with cuts through the PES signal of Fig. 6(b) (red dashed) and the RIPS signal (solid blue/gray) at polar angles (a) $\theta = 0$, (b) $\theta = 30°$, (c) $\theta = 60°$, and (d) $\theta = 90°$. The RIPS signal shown as red dashed curves in Fig. 4 is included to simplify comparison.

density, the RIPS map, and the PES map, illustrating that the PES resolution is comparable to that of RIPS and inferior compared to the analogous HHG map. The reason for the poor imaging performance of PES signals compared to HHG for this system, is a combination of two features, the elimination of either which improves the contrast. First, the dominant rotational operator in the PES signal is $\cos^2\theta \sin^2\theta$, which peaks in the z-y plane. Due to that lack of ϕ dependence for this operator, integration over ϕ averages out the details, leading to a loss of contrast. Thus, if one uses, for instance, the dipole matrix elements of N_2, instead of those of O_2 (with all other parameters retained as those corresponding to O_2), ϕ integration leads to insignificant azimuthal angle averaging leading to very good contrast (results not shown here). Thus, the symmetry of the bound orbital determines if and to what extent azimuthal averaging will degrade the contrast. Second, since, as discussed above, low angular momenta of the continuum electronic wave function are associated, via angular momentum conservation, with low-order rotational operators (ones that include low powers of trigonometric functions and are hence less well localized in angular space), the dominance of the lowest partial wave in the calculations leading to Fig. 6(b) limits the attainable contrast. Thus, we found that even when a single but higher photoelectron partial wave is used in calculation (e.g., the $l = 1(3), l' = 3(1)$ rather than the $l = l' = 1$ term) the contrast of the map improves. Finally, we remark that the availability of the emission direction as an experimentally tunable parameter in PES provides an opportunity to probe different rotational operators, but (depending on the form and combination of the rotational operators involved) may either improve or degrade the contrast of the image [56].

V. SUMMARY AND CONCLUSIONS

Our goal in the research described in the previous sections was to introduce and explore theoretically and numerically an approach for imaging rotational probability distributions, hence rotational coherences and their evolution in time and space. While developing the concept of rotational imaging as part of the general, and fundamentally valuable, field of wave-function imaging, we attempted to focus on experimental realizations that only slightly extend, or differently analyze, established experimental methods. As such, we considered three approaches: an extension of strong pump laser Raman-induced polarization spectroscopy (RIPS), high harmonic generation (HHG) from aligned molecules, and angle-resolved photoelectron spectroscopy (PES). The extended RIPS approach offers the advantages of simplicity of analysis and generality, the quality of the mapping being independent of the system. Numerically and analytically it was shown to capture the basic features of the rotational probability distribution while entailing a certain degree of coarse graining. Both HHG and PES offer the potential to generate better resolved images than the RIPS method, mapping both the gross features and the fine details of the rotational probability distribution, hence a direct map of high-order rotational coherences. These techniques, however, do not share the generality of RIPS nor its simple analysis, as the quality of the mapping depends not only on the geometry of the experiment but also on the molecule and its electronic structure.

In essence, the extended RIPS method provides a $P_2(\cos\theta)$-weighted measure of the probability density [$P_2(\cos\theta)$ being a Legendre polynomial of order 2], hence probing second-order rotational coherences. HHG and PES, by contrast, introduce higher-order rotational expectation values through the involvement of higher angular momentum electrons in the underlying physical process, and therefore contain information regarding higher-order rotational coherences, hence the potential for higher resolution at the cost of loss of generality and simplicity. The latter two approaches differ in detail, since the HHG rotational expectation values depend on both the angular momentum of the tunnel-ionized electronic partial wave and that of the recombining one, whereas the PES analogs contains information regarding the angular momentum of a single continuum electron partial wave.

With the concept of rotational wave-packet imaging established via the simplest case scenario of a diatomic molecule, it will be an interesting challenge for future research to extend the approach to the richer case of general, nonlinear molecules. As discussed in the previous sections, rotational wave-packet imaging provides considerably more information than the conventional $\langle\cos^2\theta\rangle$ measure (although it does not share the convenient transferability of the latter observable) while offering generality and simplicity as compared to the (already established) Coulomb imaging technique. Much more interestingly, as a sensitive probe of rotational coherences, the imaging approach provides potentially a probe of both intramolecular rotational perturbations (such as Coriolis and centrifugal couplings) and the response of rotational modes to different media. Finally, an experimental study of the mapping introduced above would be clearly exciting.

ACKNOWLEDGMENTS

We are grateful to the U.S. Department of Energy (Grant No. DE-FG02-04ER15612) for support.

APPENDIX: DENSITY-MATRIX APPROACH TO PES SIGNALS

The Hamiltonian of the molecular system can be simplified as comprising an active bound electronic state and an electronic continuum with their respective associated vibrational and rotational manifolds as

$$H_0 = \sum_{\{b\}} E^{\{b\}} |\{b\}\rangle\langle\{b\}| + \sum_{\{c\}} \int d\vec{k}\, E^{\{c\}} |\vec{k},\{c\}\rangle\langle\vec{k},\{c\}|, \tag{A1}$$

where all variables are defined in Sec. III C. The interaction of the ionizing (probe) pulse $\vec{\varepsilon}_{\rm pr}(t)$ with the molecular dipole vector operator $\vec{\mu}$ can be expressed as

$$H_{\rm int}(t) = -\sum_{\{c\}\{b\}} \int d\vec{k}\, \mu_{\{b\},\vec{k}\{c\}} |\{b\}\rangle\langle\vec{k},\{c\}| \varepsilon_{\rm pr}(t) + \text{H.c.}, \tag{A2}$$

where

$$\mu_{\{b\},\vec{k}\{c\}} = \langle\{b\}|\vec{\mu}\cdot\hat{\varepsilon}_{\rm pr}|\vec{k},\{c\}\rangle, \tag{A3}$$

and the probe pulse has been written as $\vec{\varepsilon}_{\rm pr}(t) = \hat{\varepsilon}_{\rm pr}\varepsilon_{\rm pr}(t)$, $\hat{\varepsilon}_{\rm pr}$ being a unit vector in the direction of polarization of the probe pulse. The coherent quantum Liouville equation for the molecular density operator $\tilde{\rho}(\tau,t)$ is given in terms of Eqs. (A1) and (A2) as

$$\frac{d\tilde{\rho}(\tau,t)}{dt} = -\frac{i}{\hbar}\left[H_0 + H_{\rm int}, \tilde{\rho}(\tau,t)\right]. \tag{A4}$$

Expanding the molecular density operator in terms of the relevant bound and continuum states, one obtains from the quantum Liouville equation an equation of motion for the density-matrix element pertaining to the population of a continuum state $|\vec{k},\{c\}\rangle$ as

$$\frac{d\rho_{\vec{k}\{c\},\vec{k}\{c\}}(\tau,t)}{dt} = -\frac{i}{\hbar}\sum_{\{b\}}\mu_{\{b\},\vec{k}\{c\}}\varepsilon_{\rm pr}(t)\rho_{\vec{k}\{c\},\{b\}}(\tau,t) + \text{H.c.} \tag{A5}$$

Integrating Eq. (A5) over time leads to Eq. (19), where the density-matrix element for the continuum state population is given in terms of the coherences between the bound and continuum electronic states, $\rho_{\vec{k}\{c\},\{b\}}(\tau,t)$. The latter elements are given through the quantum Liouville equation as

$$\begin{aligned}\frac{d\rho_{\vec{k}\{c\},\{b\}}(\tau,t)}{dt} &= -\frac{i}{\hbar}(E^{\{c\}} - E^{\{b\}})\rho_{\vec{k}\{c\},\{b\}}(\tau,t) \\ &+ \frac{i}{\hbar}\sum_{\{b'\}}\mu_{\vec{k}\{c\},\{b'\}}\varepsilon_{\rm pr}(t)\rho_{\{b'\}\{b\}}(t) \\ &- \frac{i}{\hbar}\sum_{\{c'\}}\int d\vec{k}'\,\mu_{\vec{k}'\{c'\}\{b\}}\varepsilon_{\rm pr}(t)\rho_{\vec{k}\{c\},\vec{k}'\{c'\}}(t).\end{aligned} \tag{A6}$$

Ignoring the third term, as $\rho_{\vec{k}\{c\},\vec{k}'\{c'\}}(t) \ll \rho_{\{b'\},\{b\}}(t)$ for below saturation probe intensities, one obtains Eq. (20).

[1] J. Itatani, J. Levesque, D. Zeidler, H. Niikura, H. Pepin, J. C. Kieffer, P. B. Corkum, and D. M. Villeneuve, Nature (London) **432**, 867 (2004).

[2] D. Shafir, Y. Mairesse, D. M. Villeneuve, P. B. Corkum, and N. Dudovich, Nat. Phys. **5**, 412 (2009).

[3] C. Vozzi, M. Negro, F. Calegari, G. Sansue, M. Nisoli, S. De Sivestri, and S. Stagira, Nat. Phys. **7**, 822 (2011).

[4] L. Ph. H. Schmidt, T. Jahnke, A. Czasch, M. Schöffler, H. Schmidt-Böcking, and R. Dörner, Phys. Rev. Lett. **108**, 073202 (2012).

[5] A. Monmayrant, B. Chatel, and B. Girard, Phys. Rev. Lett. **96**, 103002 (2006).

[6] K. Ohmori, Annu. Rev. Phys. Chem. **60**, 487 (2009).

[7] T. J. Dunn, I. A. Walmsley, and S. Mukamel, Phys. Rev. Lett. **74**, 884 (1995).

[8] C. Leichtle, W. P. Schleich, I. Sh. Averbukh, and M. Shapiro, Phys. Rev. Lett. **80**, 1418 (1998).

[9] T. C. Weinacht, J. Ahn, and P. H. Bucksbaum, Phys. Rev. Lett. **80**, 5508 (1998).

[10] T. C. Weinacht, J. Ahn, and P. H. Bucksbaum, Nature (London) **397**, 233 (1999).

[11] E. Skovsen, H. Stapelfeldt, S. Juhl, and K. Mølmer, Phys. Rev. Lett. **91**, 090406 (2003).

[12] P. F. Tekavec, T. R. Dyke, and A. H. Marcus, J. Chem. Phys. **125**, 194303 (2006).

[13] R. E. Carley, E. D. Boléat, R. S. Minns, R. Patel, and H. H. Fielding, J. Phys. B **38**, 1907 (2005).

[14] S. Haessler, J. Caillat, W. Bontu, C. Giovanetti-Teixeira, T. Ruchon, T. Augste, Z. Diveki, P. Berger, A. Maquet, B. Carré, R. Taïeb, and P. Salières, Nat. Phys. **6**, 200 (2010).

[15] H. Katsuki, H. Chiba, B. Girard, C. Meier, and K. Ohmori, Science **311**, 1589 (2006).

[16] H. Katsuki, H. Chiba, C. Meier, B. Girard, and K. Ohmori, Phys. Chem. Chem. Phys. **12**, 5189 (2010).

[17] Th. Ergler, A. Rudenko, B. Feuerstein, K. Zrost, C. D. Schröter, R. Moshammer, and J. Ullrich, Phys. Rev. Lett. **97**, 193001 (2006).

[18] I. A. Bocharova, H. Mashiko, M. Magrakvelidze, D. Ray, P. Ranitovic, C. L. Cocke, and I. V. Litvinyuk, Phys. Rev. A **77**, 053407 (2008).

[19] S. De, I. A. Bocharova, M. Magrakvelidze, D. Ray, W. Cao, B. Bergues, U. Thumm, M. F. Kling, I. V. Litvinyuk, and C. L. Cocke, Phys. Rev. A **82**, 013408 (2010).

[20] S. De, M. Magrakvelidze, I. A. Bocharova, D. Ray, W. Cao, I. Znakovskaya, H. Li, Z. Wang, G. Laurent, U. Thumm, M. F. Kling, I. V. Litvinyuk, I. Ben-Itzhak, and C. L. Cocke, Phys. Rev. A **84**, 043410 (2011)

[21] For a review, see H. Stapelfeldt and T. Seideman, Rev. Mod. Phys. **75**, 543 (2003).

[22] For a recent review, see T. Seideman and E. Hamilton, Adv. At. Mol. Phys. **52**, 289 (2006).

[23] F. Rosca-Pruna and M. J. J. Vrakking, Phys. Rev. Lett. **87**, 153902 (2001).

[24] I. V. Litvinyuk, K. F. Lee, P. W. Dooley, D. M. Rayner, D. M. Villeneuve, and P. B. Corkum, Phys. Rev. Lett. **90**, 233003 (2003).

[25] P. W. Dooley, I. V. Litvinyuk, K. F. Lee, D. M. Rayner, M. Spanner, D. M. Villeneuve, and P. B. Corkum, Phys. Rev. A **68**, 023406 (2003).

[26] V. Renard, M. Renard, S. Guérin, Y. T. Pashayan, B. Lavorel, O. Faucher, and H. R. Jauslin, Phys. Rev. Lett. **90**, 153601 (2003).

[27] V. Renard, M. Renard, A. Rouzee, S. Guèrin, H. R. Jauslin, B. Lavorel, and O. Faucher, Phys. Rev. A **70**, 033420 (2004).

[28] H. Hasegawa and Y. Ohshima, Phys. Rev. A **74**, 061401(R) (2006).

[29] H. Hasegawa and Y. Ohshima, Phys. Rev. Lett. **101**, 053002 (2008).

[30] E. R. Peterson, C. Buth, D. A. Arms, R. W. Dunford, E. P. Kanter, B. Krässig, E. C. Landahl, S. T. Pratt, R. Santra, S. H. Southworth, and L. Young, Appl. Phys. Lett. **92**, 094106 (2008).

[31] Y. Feng, H. Pan, J. Liu, C. Chen, J. Wu, and H. Zeng, Opt. Express **19**, 2852 (2011).

[32] J. Wu, H. Cai, Y. Tong, and H. Zeng, Opt. Express **17**, 16300 (2009).

[33] F. Krausz and M. Y. Ivanov, Rev. Mod. Phys. **81**, 163 (2009).
[34] J. J. Larsen, I. Wendt-Larsen, and H. Stapelfeldt, Phys. Rev. Lett. **83**, 1123 (1999).
[35] M. G. Reuter, M. Sukharev, and T. Seideman, Phys. Rev. Lett. **101**, 208303 (2008).
[36] M. G. Reuter, M. A. Ratner, and T. Seideman, Phys. Rev. A **86**, 013426 (2012).
[37] T. Seideman, J. Chem. Phys. **107**, 7859 (1997).
[38] K. L. Reid, T. A. Field, M. Towrie, and P. Matousek, J. Chem. Phys. **111**, 1438 (1999).
[39] S. C. Althorpe and T. Seideman, J. Chem. Phys. **113**, 7901 (2000).
[40] T. Seideman and S. C. Althorpe, J. Electron Spectrosc. Relat. Phenom. **108**, 99 (2000).
[41] T. Seideman, Annu. Rev. Phys. Chem. **53**, 41 (2002).
[42] K. L. Reid, Int. Rev. Phys. Chem. **27**, 607 (2008).
[43] S. Ramakrishna and T. Seideman, Phys. Rev. Lett. **95**, 113001 (2005).
[44] S. Ramakrishna and T. Seideman, J. Chem. Phys. **124**, 034101 (2006).
[45] J. S. Baskin, P. M. Felker, and A. H. Zewail, J. Chem. Phys. **84**, 4708 (1986).
[46] C. Riehn, Chem. Phys. **283**, 297 (2002).
[47] J. Lindgren, E. Hulkko, M. Pettersson, and T. Kiljunen, J. Chem. Phys. **135**, 224514 (2011).
[48] Y. Suzuki and T. Seideman, J. Chem. Phys. **122**, 234302 (2005).
[49] P. B. Corkum, Phys. Rev. Lett. **71**, 1994 (1993).
[50] M. Lewenstein, Ph. Balcou, M. Y. Ivanov, A. L'Huillier, and P. B. Corkum, Phys. Rev. A **49**, 2117 (1994).
[51] S. Ramakrishna and T. Seideman, Phys. Rev. Lett. **99**, 113901 (2007).
[52] S. Ramakrishna and T. Seideman, Phys. Rev. A **77**, 053411 (2008).
[53] R. M. Lock, S. Ramakrishna, X. Zhou, H. C. Kapteyn, M. M. Murnane, and T. Seideman, Phys. Rev. Lett. **108**, 133901 (2012).
[54] P. A. J. Sherratt, S. Ramakrishna, and T. Seideman, Phys. Rev. A **83**, 053425 (2011).
[55] D. A. Horke, A. S. Chatterley, and J. R. R. Verlet, J. Phys. Chem. Lett **3**, 834 (2012).
[56] S. Ramakrishna and T. Seideman, J. Phys. B. **45**, 194012 (2012).
[57] T. Seideman, J. Chem. Phys. **113**, 1677 (2000).
[58] T. Seideman, Phys. Rev. A **64**, 042504 (2001).
[59] V. Blanchet, M. Zgierski, T. Seideman, and A. Stolow, Nature (London) **401**, 52 (1999).
[60] V. Blanchet, S. Lochbrunner, M. Schmitt, J. P. Shaffer, J. J. Larsen, M. Zgierski, T. Seideman, and A. Stolow, Faraday Discuss. **115**, 33 (2000).
[61] Y.-I. Suzuki, M. Stener, and T. Seideman, Phys. Rev. Lett. **89**, 233002 (2002).
[62] Y.-I. Suzuki, M. Stener, and T. Seideman, J. Chem. Phys. **118**, 4432 (2003).